Thermographic 3D particle tracking velocimetry for turbulent gas flows

Moritz Stelter, Fabio J W A Martins, Frank Beyrau, Benoît Fond

Thermographic 3D particle tracking velocimetry for turbulent gas flows

OPEN ACCESS
IOP Publishing
Measurement Science and Technology
Meas. Sci. Technol. **34** (2023) 074008 (15pp)
https://doi.org/10.1088/1361-6501/acc600

Thermographic 3D particle tracking velocimetry for turbulent gas flows

Moritz Stelter[1], **Fabio J W A Martins**[1,3], **Frank Beyrau**[1] and **Benoît Fond**[1,2,*]

[1] Institute of Fluid Dynamics and Thermodynamics, Otto von Guericke University Magdeburg, Magdeburg, Germany
[2] Department of Aerodynamics, Aeroelasticity and Acoustics (DAAA), ONERA, the French Aerospace Lab, Paris-Saclay University, Meudon, France

E-mail: benoit.fond@onera.fr

Received 14 December 2022, revised 27 February 2023
Accepted for publication 21 March 2023
Published 25 April 2023

Abstract

Turbulent flows are characterized by diverse and unsteady three-dimensional (3D) features that require 3D measurements to study. In case of non-isothermal flows, combined 3D measurements of temperature and velocity are necessary. In this paper, a thermographic 3D particle tracking velocimetry (thermographic 3D-PTV) concept is introduced for simultaneous 3D temperature and velocity measurements in turbulent gas flows. It is based on sub-micron thermographic phosphor particles seeded into the flow as flow tracers with low response times of a few microseconds. To obtain each tracer's position and velocity, the measurement region is illuminated volumetrically using a double-pulse green laser and Mie-scattered light is imaged by four double-frame cameras. Following the pinhole model-based calibration of all cameras, 3D particle positions are computed for both laser pulse-times using a fast minimum line of sight reconstruction code. Three-component velocities are derived from tracking individual particles between these time steps. For simultaneous 3D thermometry, temperature dependent luminescence emissions from the same phosphor particles are exploited. These emissions are excited using a UV laser synchronized with the first green laser pulse and imaged using two cameras equipped with spectral filters for ratiometric phosphor thermometry. As a result, instantaneous 3D fields of discrete temperature and velocity measurements are obtained throughout the volume. The concept is demonstrated in a turbulent heated gas jet emerging from a circular nozzle at a particle image concentration of 0.005 particle per pixel, where the symmetry of the velocity and temperature distributions about the jet axis is successfully reconstructed.

Keywords: 3D particle tracking velocimetry, 3D thermometry, 3D velocimetry, phosphor thermometry, turbulent flows, tomography, thermographic phosphors

(Some figures may appear in colour only in the online journal)

[3] Current address: Institute for Energy and Materials Processes — Tomography, University of Duisburg-Essen, Duisburg, Germany
[*] Author to whom any correspondence should be addressed.

1. Introduction

The study of turbulent fluid flows with temperature variations is crucial to many industrial sectors reliant on convective heating or cooling, mixing or dispersion of substances, as well as to fundamental research in stratified flows occurring in the atmosphere or oceans. In turbulent flows, the transport of heat and mass is intensified by spatial and temporal fluctuations of flow velocity over a wide range of scales. Due to these fluctuations, turbulent flows are intrinsically three-dimensional (3D). To visualize and quantify the flow field, velocity measurement techniques based on seeded tracer particles have been developed. By imaging particles from multiple viewing directions, the 3D particle distribution can be reconstructed. Then, either individual particles are tracked from frame to frame in 3D particle tracking velocimetry (3D-PTV) [1] or intensity patterns created by particle ensembles are tracked in tomographic particle image velocimetry (tomographic PIV) [2]. These techniques helped to establish the basic features of turbulence and continue to pinpoint singular fluid phenomena by reveling a wealth of coherent 3D flow structures and their interactions [3, 4]. Nowadays, 3D three-component velocity measurements are possible in gas and liquid flows at both low (Hz) and high (kHz) sampling rates as well as at micrometer and meter scales [5, 6]. Additionally, temporal information can be incorporated using multi-frame or time-resolved systems improving the accuracy of 3D particle positions and velocity measurements [7–9]. This enables either to increase the amount of tracked particles at higher particle image densities while keeping the number of views constant [9] or to reduce the number of views for a less complex imaging setup [10].

Yet velocity measurements alone are often not sufficient to describe the transport of heat and mass. Especially in non-isothermal turbulent flows simultaneous scalar measurements (e.g. temperature or species concentration) are needed to draw correct conclusions and to develop appropriate models [11]. Some optical temperature imaging techniques rely on scattering or luminescence processes of molecules of the fluid phase, such as Rayleigh scattering [12] or laser induced fluorescence [13]. Their extension to 3D measurements requires either a scanning approach [14], with limited temporal resolution due to finite scan times, or a multi-view tomographic reconstruction of volumetric signals [15], which could lead to biased statistics due to low-pass filtering over unresolved turbulent fluctuations in each elemental reconstruction volume. Ultimately, for combined 3D scalar and velocity measurements using such approaches, at least two multi-view systems must be combined, typically yielding different reconstructed geometries.

Another approach, which we opt for in this study, is to use seeded particles within the flow for both 3D temperature and 3D velocity measurements. The same solid particles are then used as tracers for both the fluid temperature and the flow velocity [16]. Based on this approach, different concepts are described in the literature. In [17] and [18], microscopic astigmatism PTV was coupled with a double-frame luminescence lifetime determination of 10 µm encapsulated EuTTA particles to study a liquid micro-channel flow and the heating of a microfluidic device by surface acoustic waves, respectively. In another study by [19], 100 µm thermochromic liquid crystal particles were dispersed in a Rayleigh–Bénard convection cell filled with a water–glycol mixture. The particles were illuminated by white light and imaged by four monochrome cameras for tomographic PIV and 3D particle localization, as well as by an additional color camera with stopped-down aperture to determine temperature from their Hue value. These approaches result in scattered measurements of temperature and the three components of velocity at each 3D particle location with no temporal or spatial filtering. These measurement principles together with large tracer particles are well suited for research in liquid micro fluidics or investigations in slow macroscopic liquid flows at ambient temperatures. However, they are not applicable to macroscopic turbulent gas flows due to large temperature and velocity response times of their tracer particles in such flows.

Here, we propose to use sub-micron thermographic phosphor particles as flow tracers. Due to their small size, they follow temperature and velocity fluctuations precisely with response times in the microsecond range even in gas flows [16]. They are therefore suitable tracers for turbulent flows at high Reynolds numbers. These all-solid inorganic particles have a high thermochemical stability over a wide temperature range, with measurements reported up to 1400 K [20]. A variety of applications of these particles for point and 2D temperature measurements in liquid and gas flows is reviewed in [21]. In the present study, we extend this concept to 3D measurements using thermographic phosphor tracer particles and two-frame 3D-PTV. For this purpose, the particles are seeded into a flow and imaged using multiple cameras. Mie-scattering images of the particles are captured by four cameras for 3D particle position reconstruction and velocimetry, while the luminescence emission of the particles is simultaneously recorded using two cameras for two-view ratiometric temperature measurements. In this approach, the temperature information is derived from macroscopic images of individual sub-micron particles. This is a major challenge compared to the above-mentioned studies where large particles or microscopic imaging could afford much higher signal levels.

In the following, the experimental setup, imaging method, selection of the tracer particles, selection of the excitation wavelength, and the developed processing routines are described. Finally, measurement results of a turbulent heated gas jet are presented to demonstrate the capability of providing instantaneous 3D temperature and velocity measurements using the present technique.

2. Experimental setup

To facilitate simultaneous 3D temperature and velocity measurements in gas flows using the present concept of thermographic 3D-PTV, three main steps are necessary, as described in detail in the following sections. First, positions of seeded tracer particles are reconstructed within an illuminated measurement volume (sections 2.1, 4.1 and 4.2). Then, these

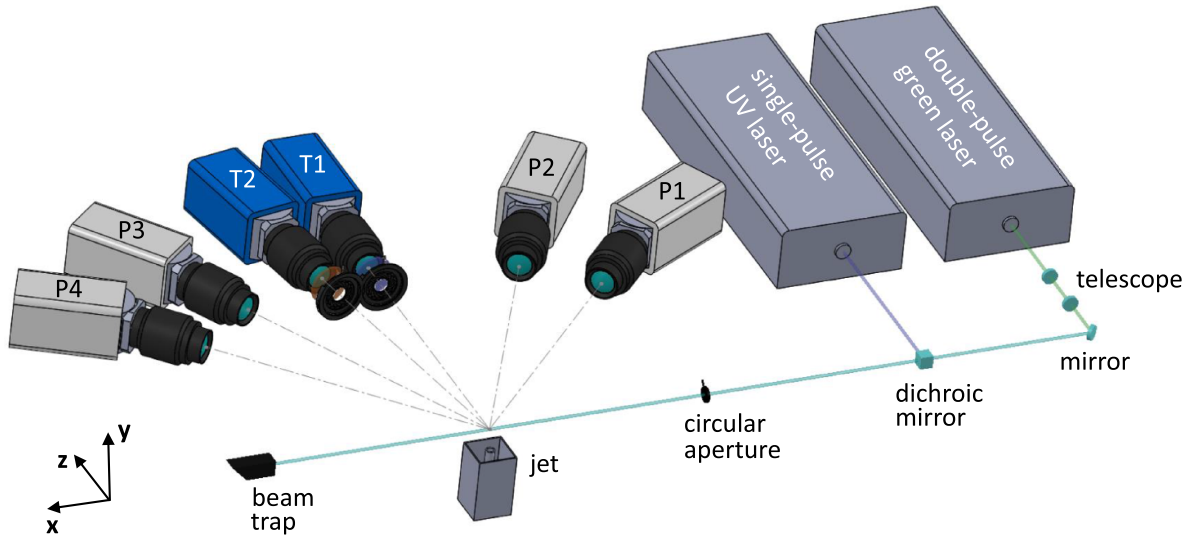

Figure 1. Schematic representation of the experimental setup consisting of six cameras, two lasers, optical components and a heated jet with co-flow. Cameras P1–P4 record Mie-scattered light from the green laser beam (532 nm) while cameras T1–T2 record luminescence emissions excited by the UV laser beam (266 nm or 355 nm).

positions are tracked over two time instants to derive particle velocity vectors (section 4.3). Finally, the luminescence emission of the same particles is evaluated to derive their temperature values (section 4.4). In this way, discrete temperature and velocity measurements are obtained at each particle position within the measurement volume. The optical setup for the present measurements is depicted in figure 1 and described in detail in the following paragraphs. It consists of six cameras divided into two groups to capture Mie scattering and luminescence emissions of the seeded tracer particles, two laser light sources to illuminate the tracers, and optical components to guide and shape the laser beams. As a test case, a heated jet with co-flow is used to provide a non-isothermal turbulent gas flow. The particles are seeded into the gas flow using a cyclone seeder, and the gas flow rates are controlled using digital mass-flow controllers.

2.1. PTV sub-system

To obtain 3D particle coordinates and velocity vectors from Mie-scattering recordings, four cameras and one double-pulse PTV laser are used. The double-pulse 10 Hz Nd:YAG laser is operated at a wavelength of 532 nm to illuminate the particles. Its beam diameter is expanded to 8 mm using a Galilean telescope to match the diameter of a second laser used to excite temperature dependent luminescence from the particles (section 2.2). The resulting Mie-scattered green light is recorded in double-frame images of cameras P1 to P4 (LaVision Imager Pro X) to allow 3D particle position reconstruction and velocity measurements using in-house algorithms (section 4). These cameras are positioned on a common horizontal plane at a distance of 715 mm to the jet at angles of 51°, 66°, 114° and 129°, where 0° is the forward scattering direction. The resulting angular aperture of 78° is sufficient for accurate 3D reconstructions, especially as the particle seeding densities targeted in this study are relatively low, i.e. below 0.01 particles per pixel (ppp) [6, 22]. The cameras are equipped with Scheimpflug adapters to account for their oblique views and 100 mm focal length objectives. Their apertures are set to $f/22$ for P1 and P2 and to $f/16$ for P3 and P4, to produce sharply focused particle images over the whole measurement volume while accounting for the directionality of Mie-scattering intensity.

2.2. Phosphor thermometry sub-system

To excite luminescence emissions from the phosphor particles for simultaneous temperature measurements, a single-pulse 10 Hz Nd:YAG laser is employed. Its UV beam (wavelength of 266 nm or 355 nm) is overlapped with the green beams using a dichroic mirror. Before entering the measurement volume, low-fluence beam edges are removed using a circular aperture. The UV laser is operated at high fluence, exceeding 200 mJ cm^{-2} in a 8 mm diameter beam, to saturate the selected phosphor Zinc oxide (ZnO) and make its emission spectrum insensitive to fluence fluctuations [23]. The selection of phosphor tracer particles is discussed in section 3.1. Normalized luminescence emission spectra of this phosphor recorded at different temperatures between 293 K and 473 K are presented in figure 2 showing the temperature-induced shift and broadening of the emission spectrum.

To exploit the change in the emission spectrum for temperature measurements, two cameras T1 and T2 (LaVision Imager sCMOS) record the luminescence emissions while equipped with 387–11 nm (Edmund Optics 84-094) and 425–50 nm (Edmund Optics 86-961) spectral filters. These filters

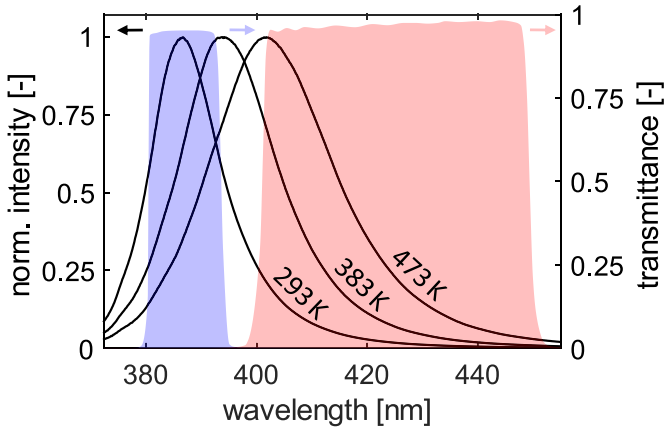

Figure 2. Normalized luminescence emission spectra of the selected phosphor ZnO recorded at three different temperatures [23] superimposed with the transmission profiles of the 387–11 nm and 425–50 nm spectral filters used with cameras T1 and T2.

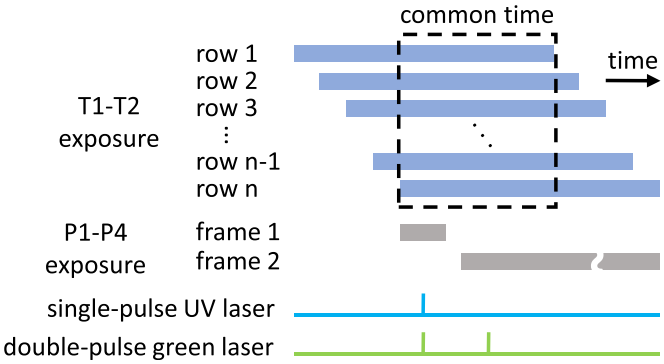

Figure 3. Timing diagram showing the correspondence between laser pulses and camera exposure times. Frames of cameras P1–P4 are synchronized with the green laser pulses to capture Mie-scattering signal. The UV laser pulse is synchronized with the first green pulse. The common exposure time of all sensor rows of cameras T1 and T2 allows to capture the luminescence emission with optimized signal-to-noise ratio in a global-shutter-like manner (despite rolling shutter operation).

are selected to match the phosphor's luminescence emission spectrum (cf figure 2). T1 and T2 are positioned on the same horizontal plane as the PTV cameras. These two cameras are seated directly next to each other, resulting in angles of 89° and 101°. They are equipped with an extension ring and a Scheimpflug adapter, respectively, to match their lens-sensor distance while accounting for the oblique view of camera T2. Objectives of 85 mm focal length are used with both cameras to match the magnification of the PTV cameras at 0.2. To maximize luminescence signal collection the apertures are fully opened to $f/1.4$. As a result, not all particles within the illuminated volume are imaged in focus with implications for the image processing, as discussed in section 4.4. External apertures (i.e. not physically connected to the objective lenses) are used with T1 and T2 to increase their depth-of-field during the camera calibration procedure (section 4.1).

2.3. Timing

To perform simultaneous temperature and velocity measurements, proper timing of the lasers and camera exposures is critical. The timing scheme employed in the present work is summarized in figure 3. The double-frame recording of cameras P1 to P4 is synchronized with the two green laser pulses to capture the particle Mie-scattering signals. The delay between the two pulses is adjusted depending on the flow conditions to maintain an average particle displacement from frame to frame of about 9 pixel. The first-frame exposure time is set to 5 µs while the second-frame exposure cannot be controlled and is much longer (millisecond range). The UV laser beam is synchronized with the first green laser pulse. To capture the resulting luminescence emissions of the particles, cameras T1 and T2 are synchronized with the UV beam. Opposed to cameras P1 to P4, cameras T1 and T2 are not operated in double-frame mode but in single-frame mode with rolling shutter. This minimizes the camera readout noise, to improve the signal-to-noise ratio of the low-intensity luminescence signal. Setting the exposure time for T1 and T2 to 35 ms and starting it 32 ms before the UV laser beam yields a common exposure time of all sensor rows of about 5 ms. However, the effective luminescence collection time is governed by the UV laser pulse duration (10 ns) as it is longer than the phosphor luminescence lifetime for this phosphor [24]. As the UV laser is fired within the common time of all sensor rows, a global-shutter-like image is obtained even in rolling shutter mode. Six simultaneous images (four Mie-scattering and two luminescence images) of the particles are recorded at the first laser pulse time (when UV and green lasers are fired simultaneously) and four Mie-scattering images are captured during the second laser pulse time (green laser only). These ten images are acquired at a measurement frequency of 5 Hz, limited by the read-out time of double-frame cameras P1–P4.

3. Selection of tracer particle and excitation wavelength

3.1. Tracer particle selection

The tracing abilities of the phosphor particles are crucial for the accuracy of this technique, as it is the temperature and velocity of the particles which is measured. The particle motion and temperature must follow the velocity and temperature fluctuations of the flow imposed by the turbulence. This requires that the momentum and thermal inertia of the particles are sufficiently small. Naturally, the temperature sensitivity of the luminescence emission has to be as high as possible in the targeted range, for example from 290 K to 490 K for the demonstration measurements in section 5. It is also important that the luminescence emission of the selected phosphor particles is spectrally well separated from either green and UV lasers to mitigate cross-talk between the detection of Mie-scattered laser light and that of the luminescence.

In terms of luminescence properties, a phosphor fulfilling these criteria is ZnO. This direct band gap semiconductor emits a fast (<1 ns) luminescent emission in the near

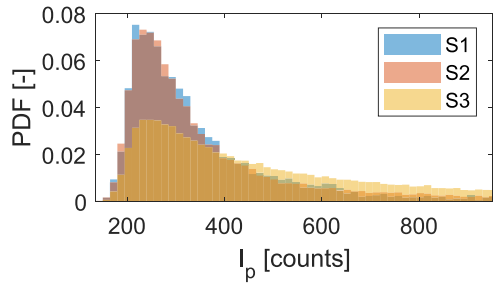

Figure 4. Probability density functions indicating the luminescence intensity emitted per particle in samples S1–S3. A minimum of 5000 particles was evaluated per sample. Colors not present in the legend result from partially overlapping histograms.

UV spectral region, which red-shifts with rising temperature due to a decreasing width of the band gap (revisit figure 2), as reported by Rodnyi and Khodyuk [24]. Excitation of this phosphor is possible with both 266 nm and 355 nm, corresponding to the fourth and third harmonic of a Nd:YAG laser.

ZnO particles are commercially available in various particle sizes and produced using different synthesize methods. Three different ZnO samples were evaluated: Sample S1 from Sigma-Aldrich (#96 479) and samples S2 and S3 from Phosphor Technology (Types GK30/UF-X and GK30/F-F1, respectively) distinguished by their specified particle size. To identify the most suitable sample, we conducted a preliminary study. The luminescence signal intensity emitted by all samples was evaluated and complemented by scanning electron microscope (SEM) images to gain an insight into particle size distributions and particle morphology. To investigate the luminescence signal, small amounts of phosphor particles were dispersed in a water-filled cuvette, excited using the 266 nm beam from a 10 Hz Nd:YAG laser while imaging the emitted luminescence using a single sCMOS camera. To maximize the particle peak intensities for easier particle image detection in this characterization study, a high magnification of 0.66 and a 300 µm thin laser sheet with a fluence of 105 mJ cm^2 were used. The luminescence emission of individual particles was evaluated for at least 5000 particles per sample. Figure 4 shows the resulting probability density functions (PDFs) of single-particle emission intensities. The distributions for all three samples peak at 240 counts. While they are very similar for samples S1 and S2, sample S3 shows a noticeably higher proportion of particles with more than 400 counts.

While brighter particles would translate to higher signal-to-noise ratios in the luminescence images, the particle size has to be considered as well as it is key for turbulent flow traceability. Therefore, SEM images of the samples were recorded at 20 kV (figure 5), and temperature and velocity response times calculated using equation (1) [25] and equation (2) [21], respectively.

$$\tau_T = d_p^2 \frac{c_{p,p}\,\rho_p}{12 k_f} \tag{1}$$

$$\tau_u = d_p^2 \frac{\rho_p}{18 \mu_f} \tag{2}$$

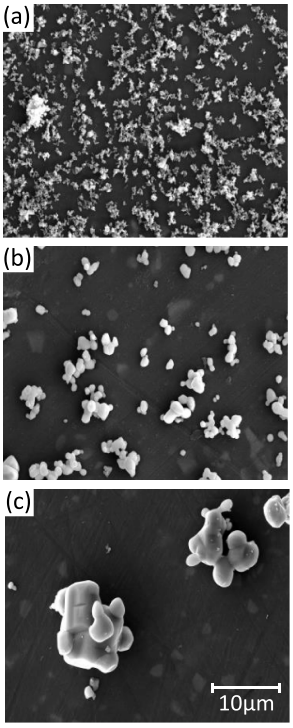

Figure 5. SEM images of ZnO samples S1–S3 (top-bottom) recorded at 20 kV show a great variation of particle shapes and sizes.

Table 1. Particle sphere-equivalent diameters and the corresponding temperature and velocity response times calculated using equations (1) and (2) for three investigated samples.

Sample	d_P (µm)	τ_T (µs)	τ_u (µs)
S1	0.6	2.42	4.90
S2	1.5	15.10	30.59
S3	10.0	670.99	1359.75

where d_p is the particle volume-equivalent diameter, $c_{p,p}$ is the particle specific heat capacity, ρ_p is the particle density, k_f is the thermal conductivity of the fluid, and μ_f is the dynamic viscosity of the fluid.

Particles in sample S1 are sub-micron flake-like structures, as reported in [26], with volume-equivalent sphere diameters of 600 nm [27]. This diameter corresponds to very low particle response times, suitable for precise tracking of turbulent flow properties, as summarized in table 1. As non-spherical particles tend to maximize drag forces resulting from surrounding fluid flow by aligning their major axis perpendicular to the flow motion, the slip velocity between particle and the fluid flow is minimized [28]. Particles in sample S2 are more spherical, which may minimize the impact of random particle orientation relative to the luminescence cameras on the measured ratio. Average particle sizes of 1–2 µm lead to response times of a few tens of microseconds, still suitable for moderate turbulence levels [29]. Sample S3 is specified with a median particle size of 4 µm, but shows much larger particles with diameters of about 10 µm, leading to response times of a few milliseconds. This is unsuitable for many turbulent gas

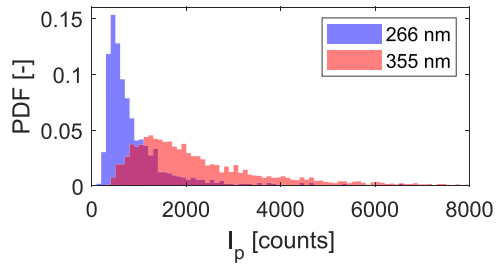

Figure 6. Histograms showing PDFs for measured particle image intensities for excitation at 266 nm and 355 nm (third color generated by a partial overlap of the histograms). Other parameters than the excitation wavelength are constant for both cases. Average particle intensities and probability for very bright particles (>2000 counts) are much higher for excitation using 355 nm.

flows, although might be a viable option in liquids. In conclusion, particles from sample S1 were selected as tracers for this study as they offer the same luminescence intensity as sample S2 but with superior temperature and velocity response times.

3.2. Excitation wavelength selection

Both 266 nm and 355 nm wavelengths can be used for excitation of ZnO. When comparing both excitation wavelengths in the context of two-dimensional measurements, it was found that 355 nm results in higher luminescence intensity over the range of 1–50 mJ cm^{-2} [26]. However, here we target a higher range of fluence, well above the saturation threshold reported by Abram *et al* in [23], and signals from individual particles are considered. Therefore, a comparison of particle intensities is necessary under the experimental conditions in our 3D measurements using both excitation wavelengths.

Particle images were taken using both 266 nm and 355 nm excitation at the same fluence and under identical detection conditions. The results are summarized in figure 6, where the intensity per particle is compared using histograms for both excitation wavelengths. Comparing the intensities where both histograms peak, using 355 nm leads to almost 3 times more signal per particle image. Additionally, the probability of very bright particle images is substantially larger using the longer excitation wavelength.

On the other hand, 355 nm excitation was reported to result in a slightly higher dependence of the ZnO emission spectrum on the excitation fluence [26] over the range of approx. 3–50 mJ cm^{-2}. This fluence dependence reduces above 60 mJ cm^{-2} [23]. To minimize this cross-dependency on the excitation laser fluence, the average fluence of the laser beam was set to 200 mJ cm^{-2} in the present study. To correct for the effect of remaining fluence variations across the laser beam cross-section on the measured intensity ratios, a flat field correction is applied as discussed in section 4.4.2.

4. Processing

To derive velocity and temperature information from raw particle image data recorded using the optical system described above (section 2), four main processing steps are required. First, the cameras are calibrated individually to establish a relationship between each two-dimensional camera image coordinate system and a common 3D world coordinate system. Second, volumes containing the particle distributions are reconstructed using both frames of the Mie-scattering images recorded by cameras P1 to P4 to derive 3D coordinates of each particle. Then, single-particle velocities are computed using the 3D particle distributions of the reconstructed volume pairs from each double-frame recording based on an in-house 3D-PTV code. Lastly, the 3D first-frame particle positions are projected into the corresponding luminescence camera images to identify the luminescence emission corresponding to each particle and to determine their temperatures.

4.1. Camera calibration

An accurate camera calibration is required to allow the computation of 3D particle coordinates from multiple two-dimensional projections, i.e. images of a particle distribution. We use a pinhole-based camera model [30] to map 3D world coordinates of a reconstructed measurement volume into two-dimensional image coordinates. A custom planar target showing a regular dot-pattern on a 5 × 5 mm^2 grid is used to establish the camera model. The target is precisely translated along the in-depth axis (z-axis, aligned with optical axis of camera T1) using a micrometer translation stage. Images are taken using all cameras at nine target positions within the volume. To increase the depth-of-field of the luminescence cameras T1 and T2 during the calibration process, the external apertures are closed to a few millimeter in diameter. For the experiments, the external apertures are fully-opened. The use of external apertures, not in physical contact with the cameras or their objective lenses, avoids that the cameras are touched during this process, mitigating movement of the imaging system and following changes to the camera calibration parameters. From the nine images recorded per camera, the internal and external camera parameters are calculated using a custom camera calibration code implemented in Matlab.

4.2. Tomographic reconstruction

Following the calibration of all cameras, the reconstruction of 3D particle positions is based on the processing of Mie-scattering images captured by cameras P1 to P4. These cameras provide images of the particle distribution within the gas flow from multiple unique viewing directions, as shown in figures 7(c)–(f). To allow the tomographic reconstruction of 3D particle positions, the illuminated measurement volume is discretized into more than 13 million cubic voxels (203 × 266 × 242) with edge lengths of 41 µm. For the relatively low particle seeding densities of <0.01 ppp in this initial demonstration of the technique, a fast non-iterative minimum line of sight (MinLOS) algorithm [31] is deemed a suitable choice and employed for the tomographic reconstruction [32]. As the seeding densities will be increased in the further development of the technique, more sophisticated reconstruction methods will be implemented.

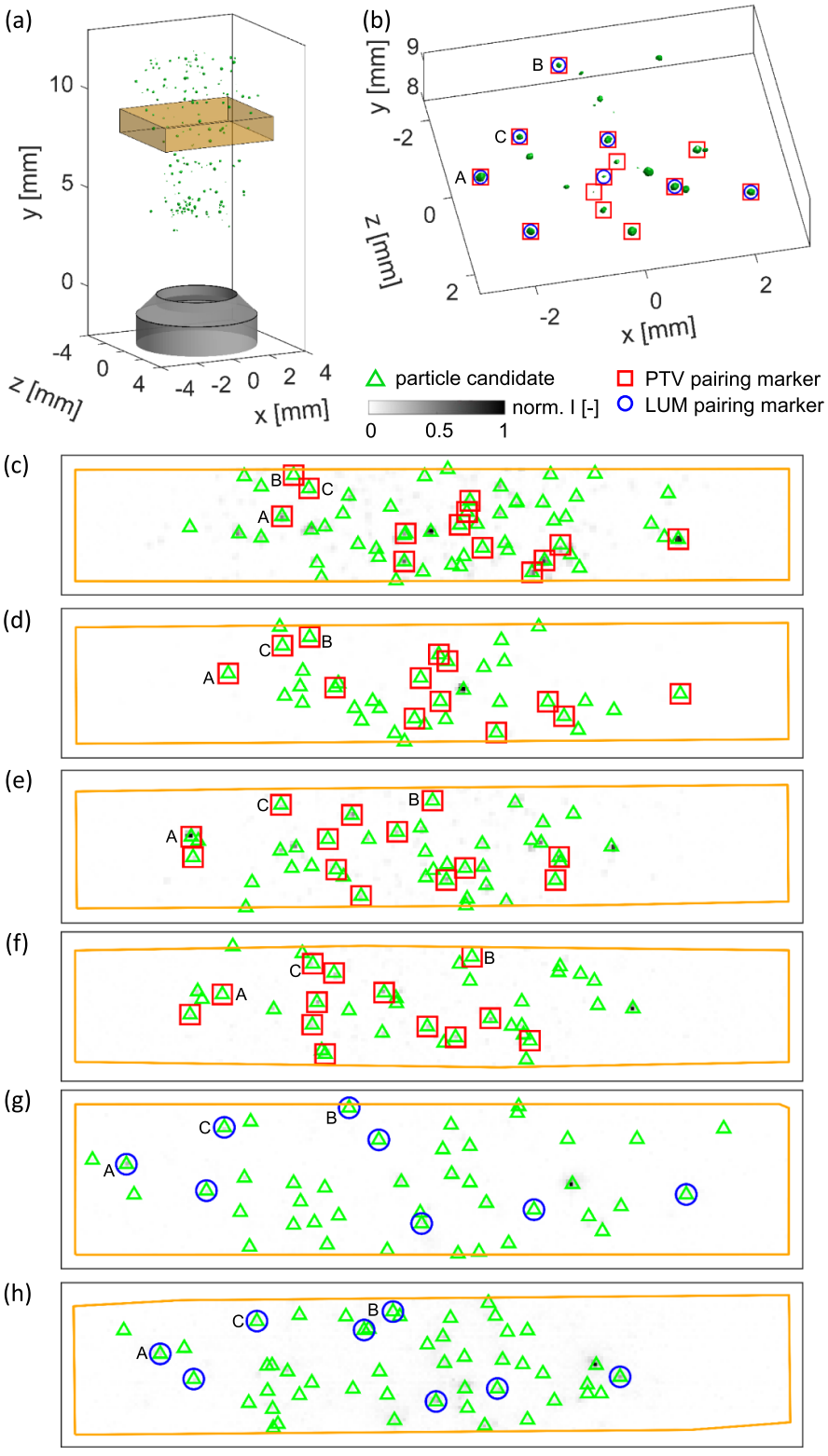

Figure 7. Reconstructed particle intensities are displayed as green iso-surface blobs in (a) and (b). The orange box in (a) indicates the sub-volume shown in (b). The corresponding regions of camera images for PTV cameras P1–P4 (c)–(f) and luminescence cameras T1 and T2 (g)–(h) are shown in normalized inverted gray scale. Markers of different color are used to indicate detected particles and successful pairing between 2D images and 3D intensity blobs. The orange bounding boxes in (c)–(h) indicate the projected limits of the sub-volume plotted in (b).

The camera images are pre-processed to aid the tomographic reconstruction process. First, an averaged background image, obtained without particles in the flow but with lasers on, is subtracted from the particle images to account for any intensity offset within the images. Then, a Gaussian smoothing of the image is performed to reduce the influence of noise. This step is followed by the identification of local intensity maxima in the images above a noise-floor threshold to provide particle candidates for the reconstruction as indicated by green triangle markers in figures 7(c)–(h). A generalized two-dimensional elliptical Gaussian function is fitted to each particle candidate to detect particle image centers with sub-pixel accuracy, as follows

$$I(x,y) = A\exp\left(-\left(\frac{\cos^2\theta}{2\sigma_x^2}+\frac{\sin^2\theta}{2\sigma_y^2}\right)(x-x_0)^2 + \left(\frac{\sin 2\theta}{2\sigma_x^2}-\frac{\sin 2\theta}{2\sigma_y^2}\right)(x-x_0)(y-y_0) - \left(\frac{\sin^2\theta}{2\sigma_x^2}+\frac{\cos^2\theta}{2\sigma_y^2}\right)(y-y_0)^2\right) \quad (3)$$

where A is the amplitude, x_0 and y_0 are the center coordinates, θ is the orientation, and σ_x and σ_y are the spreads of the blob along x and y (major and minor axis directions). Finally, identical 2D Gaussian blobs with a diameter of 3 pixels are generated at each of these detected locations, providing intensity-normalized images. This helps to reduce the influence of the beam profile of the double-pulse laser on the Mie-scattering images during the reconstruction process. As the particle images in cameras P1 to P4 are diffraction limited, a 2D Gaussian distribution is well suited to model the particle image intensity distributions (Airy disk). The luminescence images from T1 and T2 are not included in the tomographic reconstruction due to non-Gaussian character of the luminescence particle images.

From the pre-processed images, the 3D intensity distribution within the reconstructed volume is computed based on a MinLOS implementation. The center of each voxel in the volume space is projected along the lines-of-sights of the PTV cameras into their image space using the pinhole-based camera model obtained from calibration (section 4.1). A corresponding pixel intensity value of each pre-processed Mie-scattering image is computed based on the Gaussian-weighted average of the intensity of neighboring pixels at the projected image location [22]. The voxel intensities are then obtained from the minimum of the pixel intensity values. In this way, voxels with high intensity values are only created if the corresponding pixel intensities in every PTV camera image are high as well. The reconstructed volumes are smoothed and low intensity regions are zeroed resulting in 3D intensity distributions, as shown in figure 7(a).

3D particle positions are then determined by the center of gravity of connected 3D regions for sub-voxel accuracy. The 3D positions are then projected into the corresponding images of each camera to establish a pairing between reconstructed 3D particle positions and 2D camera images. Successful pairing is indicated in figures 7(b)–(h) by red square and blue circle markers for PTV and luminescence cameras, respectively. Particle candidates that are closer than 3 pixels of other neighboring particles in the image create pairing ambiguity, and are considered as unsuccessful pairing in our conservative implementation. Only those particle candidates where pairing was successful in all camera images are kept for further processing. The use of the MinLOS algorithm and our particle pairing strategy avoids some ambiguities that might occur when employing particle triangulation directly from multiple views to reconstruct 3D particle locations, e.g. while searching for corresponding particle images along epipolar lines.

As the luminescence cross-section of the particles is orders of magnitude lower than their Mie-scattering cross-section, signal levels in the luminescence images are much lower despite the lower f-stop (fully-opened apertures) of the luminescence cameras. Additionally, depth-dependent blur and aberrations in the luminescence images contribute to a broader distribution of particle image peak intensities compared to diffraction-limited Mie-scattering images. Therefore, many particles with low peak intensities cannot be detected in the luminescence images. As a result, about half as many particles are successfully paired in the luminescence images compared to the Mie-scattering counterpart.

4.3. Velocity evaluation

3D velocity vectors are computed for each individual particle. For this purpose, the Mie-scattering double-frame images recorded by cameras P1 to P4 during both green laser pulses are used. From each first-frame and second-frame image quartet particle positions are tomographically reconstructed using our MinLOS implementation, as described above in section 4.2. To derive velocities, the displacement of each particle has to be computed. Here, this is achieved by employing a two-frame 3D-PTV algorithm. A first guess for the displacement is obtained from multi-pass cross-correlation of the ensemble reconstructed volume pairs, yielding the time-averaged velocity field within the flow [33, 34]. This first guess is used to initialize the tracking of individual particles from instantaneous reconstructed volume pairs. Each particle in a first-frame volume is displaced by the initial guess at its position. This is followed by a search for the closest corresponding particle around the guessed position in the respective second-frame volume within a maximum distance of 2 voxels. This nearest neighbor approach is possible due to the low particle seeding density in the current study and the dominant streamwise velocity component. When the algorithm detects more than one particle candidate in the second frame for a particular particle from the first frame, the particle is not paired and therefore not considered in the measurements. A more sophisticated 3D-PTV method will be implemented in the future for measurements with higher particle seeding densities for solving the then non-negligible number of ambiguous

particle pairing, as discussed in section 6. To finally convert particle displacements (millimeter) to velocities (meter per second), the displacement is divided by the known time delay between the two green laser pulses. This results in discrete velocity measurements distributed in the volume.

4.4. Temperature evaluation

4.4.1. Intensity ratio derivation. To accompany each velocity vector derived according to the previous section with the corresponding temperature value, temperatures are evaluated from the same phosphor particles. Phosphor thermometry is a flexible technique for temperature measurements with different strategies to derive temperatures from temperature-dependent luminescence emissions of phosphor particles [21]. For the present technique, we chose a spectral approach based on intensity ratios. For this approach, phosphor luminescence emissions are excited using a UV laser and monitored in two different spectral regions using two separate cameras referred to as detection channels. The intensity in both channels is integrated and then the signal of one channel is divided by the signal of the other channel. As the emission spectrum changes with temperature, the resulting intensity ratio is temperature dependent. To obtain the intensity ratios in the present study, two cameras T1 and T2 are equipped with spectral filters matching the phosphor emission spectrum (cf figure 2). Particle luminescence images are pre-processed by subtracting an average background image to remove any intensity offset. As described in the previous section, reconstructed particle positions are projected into all camera images to establish a correspondence between 3D particle positions and intensity maxima in the 2D images. After identifying and pairing the particles within the camera images, the luminescence signal collected for each particle has to be determined. For this purpose, the recorded counts of all pixels contributing to each individual particle image are summed. To identify the relevant pixels for each particle image, an adaptive mask is used, as shown by the red bounding box in figure 8. To generate the mask, a generalized 2D elliptical Gaussian, described in equation (3), is fitted to each particle image. This fit allows for random orientation of particle images with respect to the image axes and blur- or aberration-induced elliptical particle images. All pixels where the fitted intensity is above 5% of the fit maximum are identified and their imaged intensities summed. To obtain the raw intensity ratio for each individual particle, the integrated intensity in T2 is divided by the corresponding intensity in T1. To correct these raw intensity ratios for effects introduced by fluence inhomogeneities in the laser cross-section, a flat field correction is performed as described in section 4.4.2.

4.4.2. Flat-field correction. Flat field corrections are necessary for two-dimensional fluid temperature measurements using thermographic phosphor particles (cf section 3.3.4 in [21]). This is to account for spatial variations in the intensity ratio caused by spatial fluence inhomogeneities and the dependence of the spectral filter transmittance on the observation angle. The flat field correction consists of a division of the raw intensity ratio field obtained in the non-isothermal test case by the intensity ratio field obtained under uniform temperature conditions. For 3D measurements, each raw intensity ratio must be corrected by a factor which is a function of the respective particle's 3D position. Therefore, a 3D ratio distribution acquired under isothermal temperature conditions is necessary. However, only a continuous flat field allows the correction of discrete intensity ratios randomly distributed within the measurement volume. To derive a continuous flat field from discrete intensity ratio measurements requires specific processing steps. First, 3D measurements are conducted in an isothermal gas jet with co-flow and the results of multiple single-shots are accumulated to generate a volume more densely populated with intensity ratios. The volume is then discretized into bins. For each bin the average intensity ratio is calculated from the contained particles. Outliers are detected before averaging, as intensity ratios deviating more than $3\,\sigma$ from the average intensity ratio, leading to the removal of 1.5% of 2900 samples. As spatial variations in the laser fluence are dominating the flat field for the present measurements using ZnO and the laser beam is collimated, fluence variations along x-direction can be neglected. As a result, the volume is not discretized in x-direction, effectively generating a 2D flat field map in the laser beam cross-section (yz-plane), as shown in figure 9. Here, the yz-plane is discretized into a grid of 29×15 rectangular bins of 300×450 µm^2. Only bins with at least 5 particles are considered.

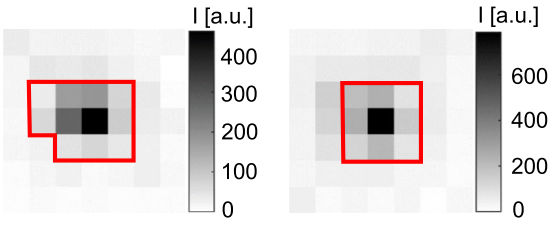

Figure 8. Sample particle image pair recorded by luminescence cameras T1 and T2 equipped with different spectral filters. The red bounding boxes correspond to the adaptive mask used for integrating the intensities.

This ratio map reflects the inhomogeneity in the laser light sheet with high ratio values corresponding to high local fluence levels. To extrapolate over regions where there are too few measurements, and to provide a smooth continuous 2D map as shown in figure 9(b), the raw map is processed using the smoothn filter implemented by Garcia [35, 36].

To correct raw intensity ratios $\varphi_{\mathrm{raw}}(x,y,z)$ measured for every particle in the volume, a correction factor $g(y,z)$ is used according to equation (4). This correction factor is the value of the 2D flat-field map (figure 9(b)) interpolated at the yz-position of the respective particle.

$$\varphi_{\mathrm{cor}}(x,y,z) = \frac{\varphi_{\mathrm{raw}}(x,y,z)}{g(x,y,z)} = \frac{\varphi_{\mathrm{raw}}(x,y,z)}{g(y,z)}. \qquad (4)$$

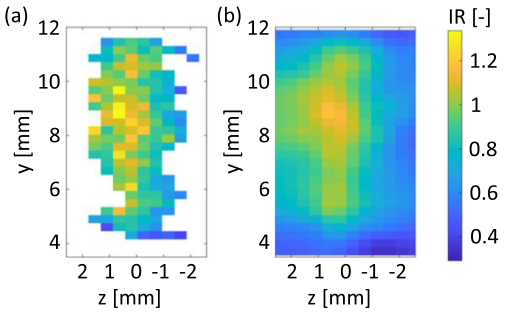

Figure 9. 2D flat-field maps obtained from 3D measurements in an isothermal jet with co-flow on a regular 2D grid, (a) before and (b) after applying the smoothn filter [35, 36].

4.4.3. Temperature calibration and conversion. To convert the corrected intensity ratios to temperature values, an *in-situ* calibration is performed in a heated nitrogen jet. To obtain the calibration data, ZnO particles are seeded into the flow fed to a nozzle of 9.5 mm diameter. 3D intensity ratio fields are measured at four different jet exit temperatures ranging from 295 K to 438 K. Measurements are taken close to the nozzle, with the measurement region starting only 2 mm above the nozzle exit, to stay within the potential core of the jet. The processing steps of sections 4.1, 4.2 and 4.4.1 are performed on the acquired data to obtain scattered 3D intensity ratios within the measurement volume. Measurements accumulated over multiple single-shots for each calibration temperature are shown in figures 10(a)–(d). As expected, the ratios of particles located in the jet core increase monotonically with increasing temperature. For the 438 K case, lower intensity ratio data points are found at the jet periphery corresponding to particles in fluid parcels cooled down by thermal mixing in the shear layer, as only the jet was seeded. For calibration of the system, the intensity ratios of all particles in a 4 mm-diameter sub-volume in the jet center are ensemble averaged to provide the calibration points shown as blue triangle markers in figure 10(e). As in [23], a power-law as defined in equation (5) is fitted to these measurement points to provide the ratio-to-temperature conversion relation.

$$\varphi(T) = p_1 + p_2 T^{p_3} \tag{5}$$

where φ denotes the intensity ratio, T is the temperature, and p_1, p_2 and p_3 are fitting coefficients.

The 4-point calibration measurements were obtained using 266 nm excitation before the excitation wavelength study (section 3.2) was conducted. However, the non-isothermal heated jet measurements presented in section 5 were performed later using 355 nm excitation to maximize signal levels. To adjust the calibration curve obtained using 266 nm excitation (figure 10(e)) to measurements taken with 355 nm excitation, a two-point re-calibration is performed. First, the average intensity ratio measured at room temperature (299 K) and 355 nm excitation is derived. Then, the original calibration curve is normalized to this value, as shown in figure 10(e). To check the validity of the adjusted calibration curve, the average intensity ratio found in the jet core at 422 K and 355 nm

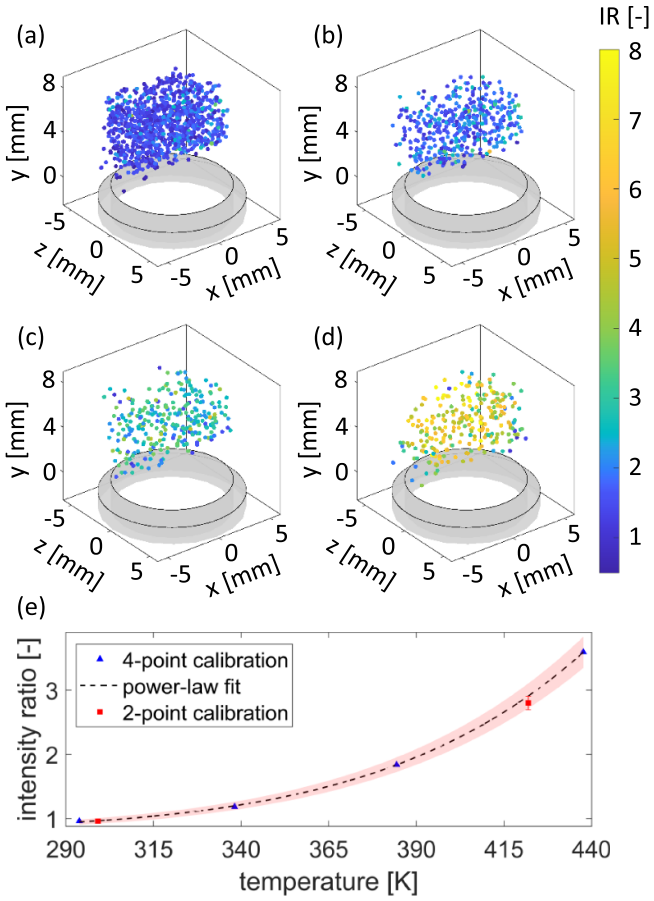

Figure 10. In (a)–(d), three-dimensional intensity ratio distributions as acquired at four different temperatures in a heated jet issuing from a nozzle of 9.5 mm in diameter are shown. The average intensity ratios, found within a 4 mm potential core region of the jet at each temperature, are used to derive a intensity-ratio-to-temperature calibration curve as shown in (e). The four calibration points obtained for the 266 nm excitation are indicated as blue triangle markers together with a dashed-line representing the derived calibration curve. For 355 nm excitation, a two-point calibration is added as red square markers. Vertical error bars and the red-shaded area around the dashed line indicate the uncertainty in the measured intensity ratios (2σ). For details on the two-point calibration, we refer to the text below.

excitation is plotted into the same figure as well. The validity of this approach is proven as the measured intensity ratio is within the uncertainty of the adjusted calibration curve.

Together with the velocities obtained from two-frame 3D-PTV (section 4.3), this results in discrete temperature and velocity measurements distributed in a volume based on the same tracer particles.

5. Demonstration in a turbulent heated jet

To demonstrate the present technique in a turbulent non-isothermal gas flow, measurements were performed in a heated gas jet with co-flow. A nitrogen jet issued from a nozzle with circular cross-section of 4 mm in diameter. Nitrogen was

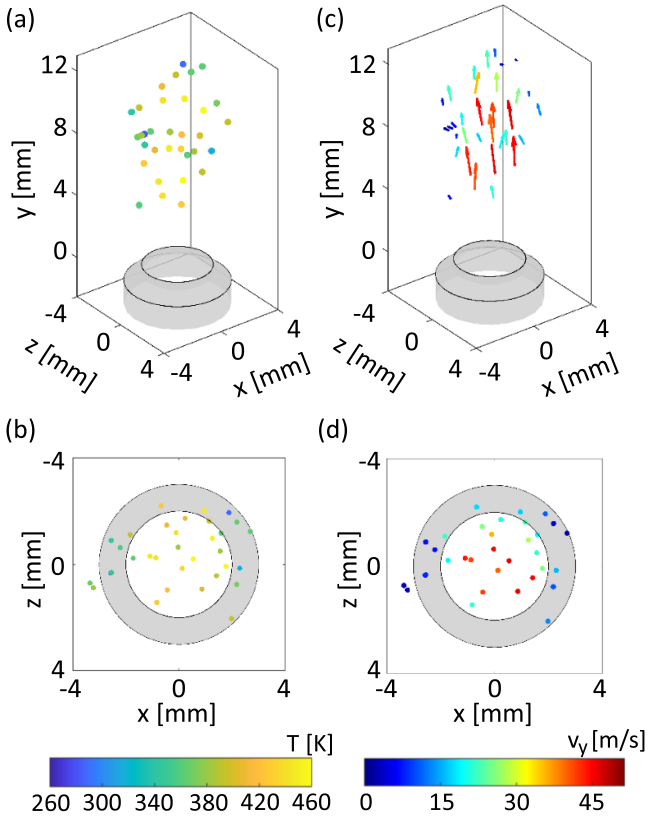

Figure 11. Sample single-shot result showing 33 discrete temperature (a), (b) and velocity (c), (d) measurements distributed in a small volume above the jet nozzle in 3D (top row) and top view (bottom row).

used for practical reasons of cylinder storage, and measurements can also be performed in air without any influence on the luminescence signal. The jet was heated to a nozzle exit temperature of 433 K at a bulk velocity of 34 m s^{-1}, resulting in a Reynolds number of 4600. The co-flow of air remained at room temperature of 300 K and a low bulk velocity of 0.2 m s^{-1}. Both streams were seeded with sub-micron ZnO particles. An example for instantaneous temperature and velocity measurements is shown in figure 11. The displayed volume is zoomed in to a small region above the jet nozzle containing 33 particles in 74 mm^3 (volume of the 3D convex hull of the particle cloud). Particles in figures 11(a) and (b) are colored in false-colors according to their temperature derived from phosphor thermometry (section 4.4), while particles and vectors in figures 11(c) and (d) are colored according to the axial velocity component computed from two-frame 3D-PTV (section 4.3). The particles closest to the jet exit center ($[x, y, z] = [0, 0, 0]$) indicate flow temperatures close to the nozzle exit temperature, and their velocities are the highest. Their velocities exceed the bulk velocity as expected from the velocity profile of turbulent pipe flows, as detailed below. Particles that are further away from the origin indicate colder flow temperatures as a result of thermal mixing. Note that to reconstruct this measurement volume, only a sub region of the image sensors corresponding to approx. 3% of the sensor area was exploited. This is due to difficulties in obtaining homogeneous seeding over both the central jet and the co-flow region. Extrapolating the particle quantity for this small region to the whole field of view of the cameras would result in more than 1200 individual temperature-velocity measurements.

Besides instantaneous measurements from single snapshots, dense temperature and velocity distributions are obtained from evaluating many instantaneous image data-sets, as shown in figure 12. Here, 3100 particles distributed in a volume of 213 mm^3 are evaluated, corresponding to approximately 14.6 particles mm^{-3}. Temperature (a)–(c) and velocity (d)–(f) results are shown in 3D plots, in top-view and in height vs radial distance from jet center scatter plots. Particles and vectors are plotted in false-colors according to their temperature (a)–(c) and axial velocity magnitude (d)–(f), respectively. To reveal the inner core structure of the jet, the 3D plots are cut-open, as indicated by the green bounding box, to show only particles in negative z-direction. The fast and hot jet core is clearly seen in these sliced 3D views. The velocity data shows excellent symmetry about the jet axis with a relatively uniform velocity magnitude in the core region of 2.5 mm in diameter.

The radial profile of the dominating streamwise velocity component (averaged over time, and vertical and azimuthal directions) is plotted in figure 13. Vertical error bars refer to one standard deviation of measured streamwise velocities and the jet nozzle position is indicated. The measured profile is compared to the velocity profile predicted for turbulent pipe flows using the one-seventh power-law [37], as calculated based on the measured gas mass flow provided to the jet. Within the core region of 2.5 mm in diameter, PTV and mass-flow-derived velocities agree with each other with an average difference of 7.8%. Within this region, the mass-flow-derived velocity is slightly lower than the average velocity from PTV measurements. This could be due to an underestimation of the jet exit temperature measured by a thermocouple due to conduction losses. This temperature is used to convert the measured gas mass flow (supplied to the jet) to the respective volume flow and bulk velocity at the jet nozzle exit, which serves as input for the calculation of the velocity profile with the one-seventh power-law. Moving to larger radial distances, the measured velocity magnitude drops steeply towards ambient co-flow velocities within a shear layer. Within this shear layer, the error bars for the measured velocities are larger than in the jet core or co-flow region, indicating a larger spread in velocity magnitude. Nevertheless, the measured gradient is lower than predicted by the one-seventh power-law due to jet spreading, turbulent mixing at the shear layer, and the absence of a wall in the free stream compared to a pipe flow. As the inter-frame time in between the PTV double-frame recordings was optimized for the jet velocity, particles in the co-flow are only displaced by a fraction of a voxel, increasing the velocity measurement uncertainty outside the jet region.

The temperature data shows a similar axis symmetry but the data is more noisy, as observed in figure 12. This is with no post-processing filters applied. High temperature data points are grouped within the central region of the jet. Similar to

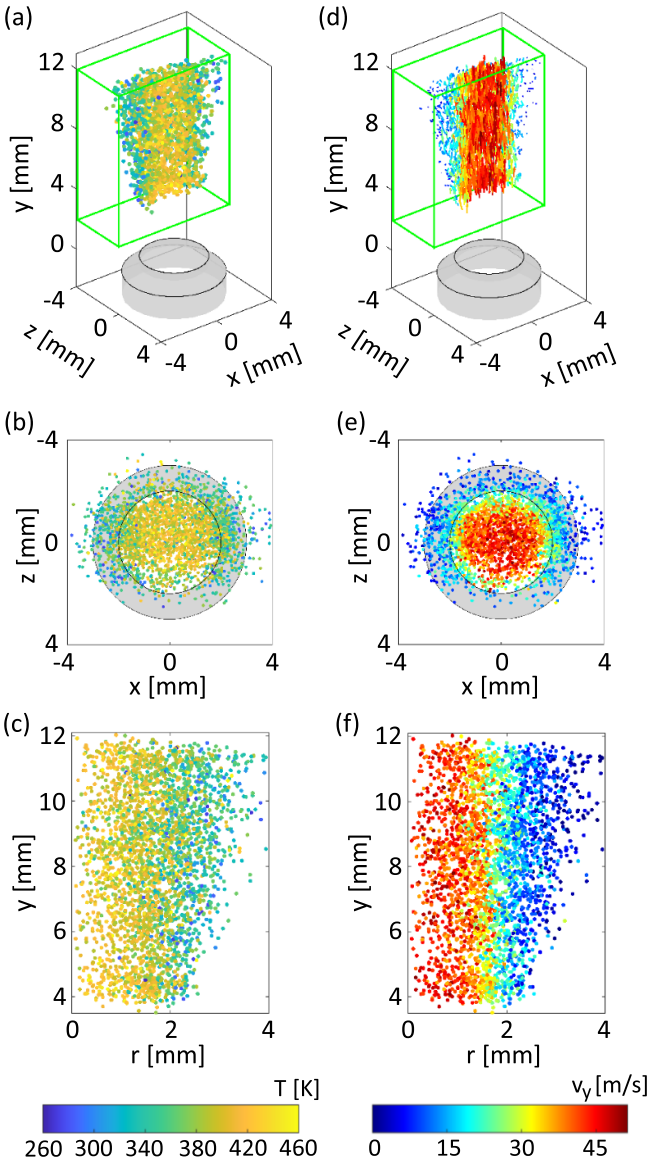

Figure 12. Cumulative results of dense measurements from more than 3100 particles in a small region above the jet nozzle. Particles are plotted in false-colors according to their temperature (a)–(c) and axial velocity magnitude (d)–(f). Multiple views are presented, including sliced 3D views to show the internal core structure, top views and radial distance from the jet center vs height scatter plots.

the velocity results, particles indicating intermediate flow temperatures are found in the shear layer where thermal mixing between both streams occurs. Only very few cold temperature points matching the co-flow exit temperature are found as a result of the lower concentration of seeding particles in the co-flow stream. An estimate for the particle-to-particle temperature and velocity precision is taken as the root mean square deviation of the distributions evaluated in the 2.5 mm-diameter jet core region as 27.4 K and 4.5 m s^{-1}, respectively. However, this also includes inherent turbulent fluctuations of both quantities at the jet exit and is therefore a worst-case estimate.

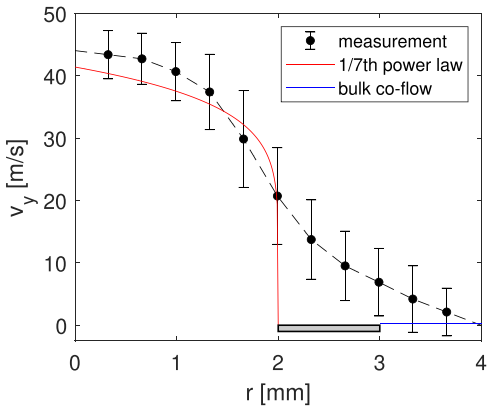

Figure 13. Radial velocity profile as derived from cumulative results. Velocities are evaluated in 0.5 mm wide bins with 33% overlap. A piecewise linear interpolation is applied to visualize the profile. This is compared to the velocity profile predicted for turbulent pipe flows by the one-seventh power-law [37] at the jet exit and the bulk velocity of the co-flow.

6. Discussion of particle seeding limit

The present results of the heated gas jet with co-flow demonstrate the applicability of the developed technique for simultaneous temperature and velocity measurements in turbulent gas flows. Higher particle seeding densities, distributed homogeneously over the whole measurement volume will improve the results in the future. The low particle seeding density (0.005 ppp) helped minimizing positioning errors resulting from moderate 3D calibration errors (0.3 pixel) and the use of a non-iterative reconstruction algorithm (average reconstruction error of 0.5 pixel) during the development of the technique. Here, only a sub-region of the camera image sensors was exploited, as homogeneous seeding could only be obtained in the jet. Improving the seeding of the gas flow would allow using the full camera frame, and the number of measurements per shot would increase to over 1200 particles. Future improvements will allow using higher particle seeding densities to increase the spatial resolution of the technique in the instantaneous measurements. More advanced reconstruction algorithms can handle particle images with seeding densities exceeding 0.1 ppp, as reported by Michaelis *et al* in [32]. However, the particle image size in the luminescence images is larger than the diffraction limited Mie-scattering images normally used for tomographic reconstruction, cf figure 8. This may impose an upper limit on the particle seeding density if only non-overlapping particle images are considered usable. Virtual particle images are used here to estimate the influence of this consideration on the maximum seeding density. For this purpose, synthetic volumes of $70 \times 70 \times 7$ mm^3 are generated and filled with random particle distributions at multiple seeding densities ranging from 0.001 to 0.05 ppp. The relation between particle z-positions in the volume and the corresponding particle image diameter in the luminescence images is derived from measurements in an isothermal jet. Particle diameters are evaluated as $2(\sigma_x + \sigma_y)$ of the 2D elliptical

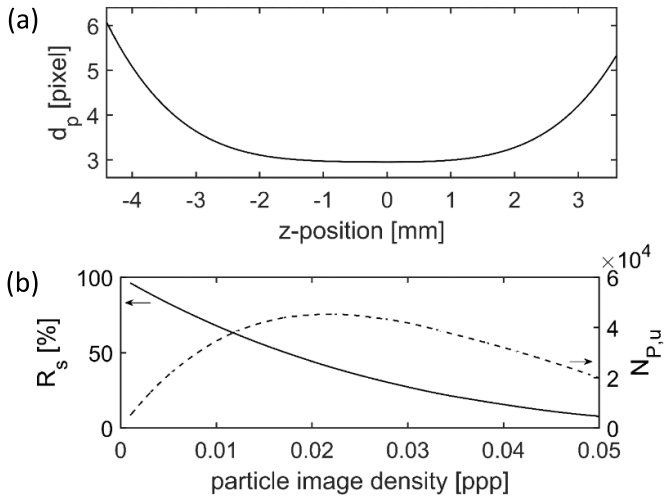

Figure 14. Relation between particle z-positions and luminescence particle image diameter d_p (a). The particle image diameter is derived as $2(\sigma_x + \sigma_y)$ from 2D Gaussian fits applied to particle images recorded in an isothermal gas jet. The maximum particle seeding density (b) is determined by evaluating multiple particle seeding densities for the number of unambiguously identifiable, non-overlapping particles $N_{P,u}$ and the separation ratio R_s.

Gaussian fit applied to particle images (section 4.2). The resulting function is shown in figure 14(a). Artificial luminescence images are generated from the synthetic volumes by modeling each particle image as a circle with a diameter according to this relation. In the resulting images the number of usable particles and the separation ratio is evaluated. The separation ratio R_s is defined as ratio between unambiguously identifiable, non-overlapping particle images with respect to the total number of particles. The results are presented in figure 14(b). An optimum is observed at a particle image density of 0.022 ppp, which is below the above mentioned limit of advanced 3D particle reconstruction algorithms. Increasing the particle seeding density beyond this level leads to lower numbers of usable particles due to increasing overlap of individual particle images. Implementing volume self-calibration [38, 39] and advanced iterative volume reconstruction algorithms [40–43] will allow us to process images at this seeding density, offering an approximated improvement in spatial measurement density by a factor of almost 4.5 compared to the current results. The use of a high-speed PTV sub-system can allow for time-resolved 3D-PTV [9, 44], leading to more accurate particle position reconstructions, velocity measurements, and with the possibility of supplementary acceleration measurements. However, performing the thermometry measurements at high-speed would require pulse-burst UV lasers [45] to provide sufficient energy for luminescence excitation for the thermometry sub-system. Additionally, the use of advanced iterative volume reconstruction algorithms and/or time-resolved 3D-PTV will potentially allow to reduce the number of cameras in the PTV sub-system, making the overall setup simpler and less expensive.

7. Conclusions

In the present work, we introduce thermographic 3D-PTV as a new technique for simultaneous 3D temperature and velocity measurements in turbulent gas flows. It is based on imaging sub-micron thermographic phosphor tracer particles with short temperature and velocity response times seeded into the flow of investigation. The present setup is composed of six cameras and two lasers. Four cameras, operated in double-frame mode, are used together with a double-pulse green laser for tomographic reconstruction of 3D particle positions and 3D-PTV based on the Mie-scattering signal. The remaining two cameras, equipped with spectral filters and operated in single-frame mode, are used together with a single-pule UV laser to provide the temperature of individual particles using a ratiometric phosphor thermometry approach based on particle luminescence emissions. This concept allows the instantaneous measurement of temperature and all three components of velocity of turbulent flows at every reconstructed particle position within the volume, while avoiding spatial bias effects and filtering. Demonstration measurements in a heated turbulent gas jet are presented at low particle seeding density of 0.005 ppp. Single-shot results provided 33 measurements of joint temperature and three-component velocity distributed in a volume of 74 mm^3. Accumulated measurements with 3100 particles successfully retrieved the symmetry about the jet axis of temperature and velocity distributions.

Further research is focused on increasing the particle seeding density towards the estimated limit of 0.022 ppp to provide more measurements per unit volume. This will be achieved by implementing volume self-calibration and more advanced volume reconstruction methods while the number of cameras can potentially be reduced. Additionally, particles with a narrower size distribution, stronger luminescence emissions and less variability in the per-particle luminescence emission intensity are currently under investigation to further increase the number of temperature and velocity samples.

Data availability statement

All data that support the findings of this study are included within the article (and any supplementary files).

Acknowledgments

Funding by the Deutsche Forschungsgemeinschaft (DFG, German Research Foundation) under Project Number 427979038 is gratefully acknowledged. The authors are also thankful for technical discussions with Péter Kováts, Katharina Zähringer and Christopher Abram.

ORCID iDs

Moritz Stelter https://orcid.org/0000-0002-0376-2727

Fabio J W A Martins https://orcid.org/0000-0002-5841-4228
Frank Beyrau https://orcid.org/0000-0002-8043-7194
Benoît Fond https://orcid.org/0000-0002-8152-4126

References

[1] Pereira F, Stüer H, Graff E C and Gharib M 2006 Two-frame 3d particle tracking *Meas. Sci. Technol.* **17** 1680–92
[2] Elsinga G E, Scarano F, Wieneke B and van Oudheusden B W 2006 Tomographic particle image velocimetry *Exp. Fluids* **41** 933–47
[3] Violato D and Scarano F 2011 Three-dimensional evolution of flow structures in transitional circular and chevron jets *Phys. Fluids* **23** 124104
[4] Schröder A and Schanz D 2023 3D Lagrangian particle tracking in fluid mechanics *Annu. Rev. Phys. Mech.* **55** 511–40
[5] Discetti S and Coletti F 2018 Volumetric velocimetry for fluid flows *Meas. Sci. Technol.* **29** 042001
[6] Scarano F 2013 Tomographic PIV: principles and practice *Meas. Sci. Technol.* **24** 012001
[7] Novara M, Batenburg K J and Scarano F 2010 Motion tracking-enhanced MART for tomographic PIV *Meas. Sci. Technol.* **21** 035401
[8] Lynch K and Scarano F 2013 A high-order time-accurate interrogation method for time-resolved PIV *Meas. Sci. Technol.* **24** 035305
[9] Schanz D, Gesemann S and Schröder A 2016 Shake-the-box: Lagrangian particle tracking at high particle image densities *Exp. Fluids* **57** 70
[10] Wu Y, Wang Q and Zhao C Y 2021 A spatial-temporal algorithm for three-dimensional particle tracking velocimetry using two-view systems *Meas. Sci. Technol.* **32** 065011
[11] Warhaft Z 2000 Passive scalars in turbulent flows *Annu. Rev. Phys. Mech.* **32** 203–40
[12] Frank J H and Kaiser S A 2008 High-resolution imaging of dissipative structures in a turbulent jet flame with laser Rayleigh scattering *Exp. Fluids* **44** 221–33
[13] Peterson B, Baum E, Böhm B, Sick V and Dreizler A 2014 Evaluation of toluene LIF thermometry detection strategies applied in an internal combustion engine *Appl. Phys.* B **117** 151–75
[14] Krug D, Holzner M, Lüthi B, Wolf M, Tsinober A and Kinzelbach W 2014 A combined scanning PTV/LIF technique to simultaneously measure the full velocity gradient tensor and the 3D density field *Meas. Sci. Technol.* **25** 065301
[15] Yu T, Liu H and Cai W 2017 On the quantification of spatial resolution for three-dimensional computed tomography of chemiluminescence *Opt. Express* **25** 24093
[16] Straußwald M, Abram C, Sander T, Beyrau F and Pfitzner M 2021 Time-resolved temperature and velocity field measurements in gas turbine film cooling flows with mainstream turbulence *Exp. Fluids* **62** 1–17
[17] Massing J, Kähler C J and Cierpka C 2018 A volumetric temperature and velocity measurement technique for microfluidics based on luminescence lifetime imaging *Exp. Fluids* **59** 163
[18] Deng Z, König J and Cierpka C 2022 A combined velocity and temperature measurement with an LED and a low-speed camera *Meas. Sci. Technol.* **33** 115301
[19] Schiepel D, Schmeling D and Wagner C 2021 Simultaneous tomographic particle image velocimetry and thermometry of turbulent Rayleigh–Bénard convection *Meas. Sci. Technol.* **32** 095201
[20] Herzog J M, Witkowski D and Rothamer D A 2021 Combustion-relevant aerosol phosphor thermometry imaging using Ce,Pr:LuAG, Ce:GdPO4 and Ce:CSSO *Proc. Combust. Inst.* **38** 1617–25
[21] Abram C, Fond B and Beyrau F 2018 Temperature measurement techniques for gas and liquid flows using thermographic phosphor tracer particles *Prog. Energy Combust. Sci.* **64** 93–156
[22] Thomas L, Tremblais B and David L 2014 Optimization of the volume reconstruction for classical Tomo-PIV algorithms (MART, BIMART and SMART): synthetic and experimental studies *Meas. Sci. Technol.* **25** 035303
[23] Abram C, Fond B and Beyrau F 2015 High-precision flow temperature imaging using ZnO thermographic phosphor tracer particles *Opt. Express* **23** 19453
[24] Rodnyi P A and Khodyuk I V 2011 Optical and luminescence properties of zinc oxide (Review) *Opt. Spectrosc.* **111** 776–85
[25] Raffel M, Willert C E, Scarano F, Kähler C J, Wereley S T and Kompenhans J 2018 *Particle Image Velocimetry* (Cham: Springer)
[26] Abram C, Pougin M and Beyrau F 2016 Temperature field measurements in liquids using ZnO thermographic phosphor tracer particles *Exp. Fluids* **57** 115
[27] Fond B, Xiao C-N, T'Joen C, Henkes R, Veenstra P, van Wachem B and Beyrau F 2018 Investigation of a highly underexpanded jet with real gas effects confined in a channel: flow field measurements *Exp. Fluids* **59** 160
[28] van Wachem B, Zastawny M, Zhao F and Mallouppas G 2015 Modelling of gas–solid turbulent channel flow with non-spherical particles with large Stokes numbers *Int. J. Multiph. Flow* **68** 80–92
[29] Fond B, Abram C, Heyes A L, Kempf A M and Beyrau F 2012 Simultaneous temperature, mixture fraction and velocity imaging in turbulent flows using thermographic phosphor tracer particles *Opt. Express* **20** 22118
[30] Cornic P, Illoul C, Cheminet A, Le Besnerais G, Champagnat F, Le Sant Y and Leclaire B 2016 Another look at volume self-calibration: calibration and self-calibration within a pinhole model of Scheimpflug cameras *Meas. Sci. Technol.* **27** 094004
[31] Putze T and Maas H-G 2008 3D determination of very dense particle velocity fields by tomographic reconstruction from four camera views and voxel space tracking *The Int. Archives of the Photogrammetry, Remote Sensing and Spatial Information Sciences*
[32] Michaelis D, Novara M, Scarano F and Wieneke B 2010 Comparison of volume reconstruction techniques at different particle densities *15th Int. Symp. on Applications of Laser Techniques to Fluid Mechanics* (*Lisbon*)
[33] Meinhart C D, Wereley S T and Santiago J G 2000 A PIV algorithm for estimating time-averaged velocity fields *J. Fluids Eng.* **122** 285–9
[34] Kováts P, Martins F J W A, Mansour M, Thévenin D and Zähringer K 2020 Tomographic PIV measurements and RANS simulations of secondary flows inside a horizontally positioned helically coiled tube *Exp. Fluids* **61** 117
[35] Garcia D 2010 Robust smoothing of gridded data in one and higher dimensions with missing values *Comput. Stat. Data Anal.* **54** 1167–78
[36] Garcia D 2010 A fast all-in-one method for automated post-processing of PIV data *Exp. Fluids* **50** 1247–59
[37] De Chant L J 2005 The venerable 1/7th power law turbulent velocity profile: a classical nonlinear boundary value problem solution and its relationship to stochastic processes *Appl. Math. Comput.* **161** 463–74
[38] Wieneke B 2008 Volume self-calibration for 3D particle image velocimetry *Exp. Fluids* **45** 549–56

[39] Wieneke B 2018 Improvements for volume self-calibration *Meas. Sci. Technol.* **29** 084002
[40] Cornic P, Leclaire B, Champagnat F, Besnerais G L, Cheminet A, Illoul C and Losfeld G 2020 Double-frame tomographic PTV at high seeding densities *Exp. Fluids* **61** 23
[41] Wieneke B 2012 Iterative reconstruction of volumetric particle distribution *Meas. Sci. Technol.* **24** 024008
[42] Sciacchitano A, Leclaire B and Schroeder A 2021 Main results of the first Lagrangian particle tracking challenge *14th Int. Symp. on Particle Image Velocimetry* vol 1
[43] Novara M, Schanz D and Schröder A 2022 Shake-The-Box 3D particle tracking for two-pulse recordings *Proc. 20th Int. Symp. on the Application of Laser and Imaging Techniques to Fluid Mechanics (Lisbon, Portugal)*
[44] Jahn T, Schanz D and Schröder A 2021 Advanced iterative particle reconstruction for Lagrangian particle tracking *Exp. Fluids* **62** 179
[45] Slipchenko M N, Meyer T R and Roy S 2021 Advances in burst-mode laser diagnostics for reacting and nonreacting flows *Proc. Combust. Inst.* **38** 1533–60